Gate-Tunable Hole and Electron Carrier Transport in Atomically Thin Dual-Channel WSe$_2$/MoS$_2$ Heterostructure for Ambipolar Field-Effect Transistors

Inyeal Lee, Servin Rathi, Dongsuk Lim, Lijun Li, Jinwoo Park, Yoontae Lee, Kyung Soo Yi, Krishna P. Dhakal, Jeongyong Kim, Changgu Lee, Gwan-Hyoung Lee, Young Duck Kim, James Hone, Sun Jin Yun, Doo-Hyeb Youn, and Gil-Ho Kim*

Over the last decade, various 2D materials have been discovered and studied as promising candidates for next-generation electronics due to their unique properties such as atomically thin thickness, high mechanical strength, transparency, flexibility, etc.[1–5] Usually, graphene is widely utilized as high mobility channel and transparent electrode, whereas transition-metal dichalcogenides (TMD), such as MoS$_2$, WSe$_2$, WS$_2$, etc., are used as the switching channel with high on/off current ratio to realize field-effect-transistor (FET)-based applications.[1,3–5] Relatively, the TMDs are highly attractive due to the existence of an appropriate energy bandgap (1.2–1.8 eV) that can facilitate the development of transparent and flexible optoelectronic devices.[6,7] Recently, several different configurations of heterojunctions, fabricated by lateral and vertical stacking of various 2D materials, have been realized to enhance the electrical and photoresponse properties. These heterostructure devices have attracted extensive attention and opened up a new avenue for novel electrical and optical application devices, such as ultrahigh mobility FETs,[8,9] tunable p–n junction diodes,[10–15] solar cells,[16] and light-emitting diodes.[17] Moreover, such a heterobilayer system with a suitable thickness of the dielectric barrier can also be extended to study charge-carrier interaction phenomena,[18] such as the proximity effect,[19] drag effect,[20,21] and superfluidity.[22–26] Most of the studies based on 2D material heterostructure have focused on transport in the vertical configuration, where multiple stacking of n- or p-type TMDs

with proper alignment of the bandgap energies results in carrier transport modulated by the gate or drain bias. However, lateral carrier transport in the stacked hetero-bilayer channels (HBC), composed of n- and p-type materials, has not been reported yet, for device applications. The formation and subsequent control of an atomic-thick lateral depletion region along the junction, using a vertical electric field or optical illumination, can be exploited for novel electrical and optical properties. The ambipolar conduction in such devices is expected to be different from that of graphene or organic materials, where a unique band structure or the material properties give rise to such transport. In the case of HBCs, their ambipolar properties are expected to show improved performance in terms of on/off ratio and mobilities, which have plagued the performance of devices based on graphene and organic materials, respectively. Further, the realization of ambipolar behavior using an electric-double-layer (EDL) ion-gel gate in TMDs is not comparable to the proposed architecture due to the limitation of the EDL gel gate for practical electronics and improved functionalities, both electrical and optical, of the HBCs.[27] A precise and continuous control of the carrier concentration and lateral depletion in HBCs makes such a system quite exotic both for fundamental physics and application-oriented research.

In this work, we demonstrate a new method that enables a dual-channel FET based on a vertically stacked heterostructure of ultrathin n-type MoS$_2$ and p-type WSe$_2$ layers for the study of

Dr. I. Lee, Dr. S. Rathi, D. Lim, Dr. L. Li, J. Park, Y. Lee, Prof. G.-H. Kim
Samsung-SKKU Graphene Center
Sungkyunkwan Advanced Institute of Nanotechnology (SAINT) and
School of Electronics and Electrical Engineering
Sungkyunkwan University
Suwon 16419, Korea
E-mail: ghkim@skku.edu
Prof. K. S. Yi
Department of Physics
Pusan National University
Busan 46241, Korea
Dr. K. P. Dhakal, Prof. J. Kim
Center for Integrated Nanostructure Physics
Institute for Basic Science (IBS)
Department of Energy Science
Sungkyunkwan University
Suwon 16419, Korea

Prof. C. Lee
Department of Mechanical Engineering
Sungkyunkwan University
Suwon 16419, Korea
Prof. G.-H. Lee
Department of Material Science and Engineering
Yonsei University
Seoul 03722, Korea
Dr. Y. D. Kim, Prof. J. Hone
Department of Mechanical Engineering
Columbia University
New York, NY 10027, USA
Dr. S. J. Yun, Dr. D.-H. Youn
ICT Components and Materials Technology Research Division
Electronics and Telecommunications Research Institute
Daejeon 34129, Korea
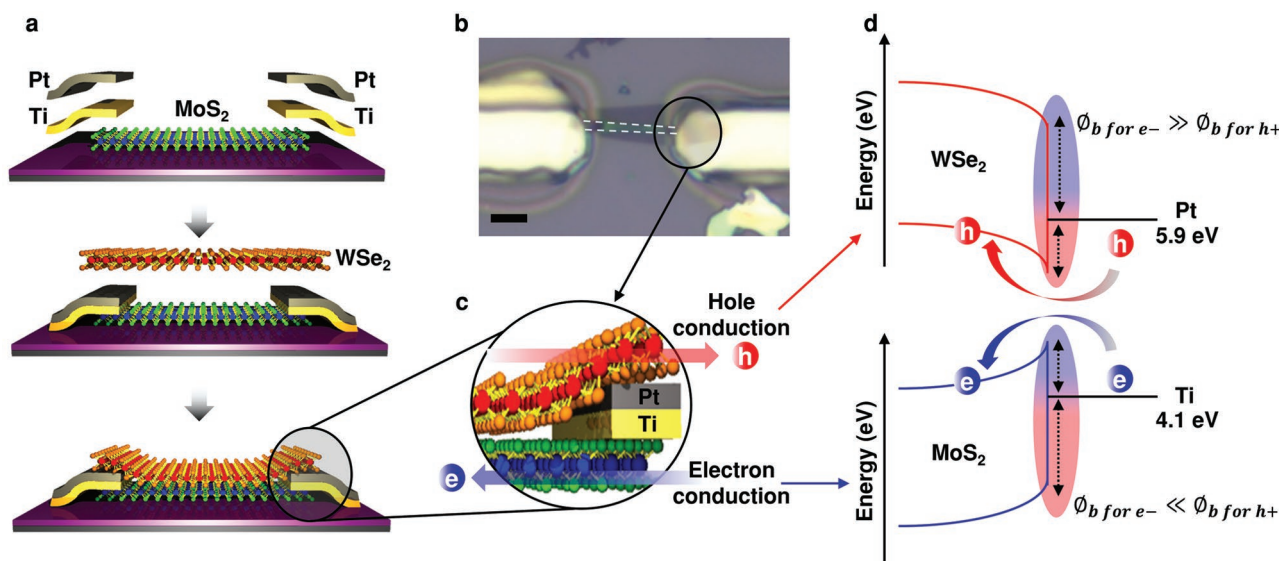
COMMUNICATION

Figure 1. Fabrication process and band diagrams of a dual-channel FET with WSe_2/MoS_2 heterostructure. a) Schematic of device fabrication process. b) Optical image of the fabricated device (scale bar = 5 µm). The white dashed line represents the bottom MoS_2 layer. c) Illustration of hole and electron transport in the individual channel of the dual-channel FET. d) Band diagrams for (top) WSe_2–Pt metal and (down) MoS_2–Ti metal. Φ_b indicates the barriers for hole and electron.

parallel carrier transport (electrons from MoS_2 and holes from WSe_2). When a WSe_2 layer was transferred onto a MoS_2 layer, the stacked device showed ambipolar behavior, which allows for additional functionality of independent gate control on individual MoS_2 (n-type) or WSe_2 (p-type) channels while maintaining the on/off ratio of $\approx 10^5$. In our device structure, both a positive and negative tunable photocurrent was observed, where the negative photocurrent was particularly enhanced by the electron–hole recombination at the heterointerface of a MoS_2–WSe_2 planar junction formed by direct contact without a barrier.

The device-fabrication process is depicted in **Figure 1**a and Figure S1 (Supporting Information) (see the Experimental Section and Section S1, Supporting Information, for details). First, a MoS_2 layer was mechanically exfoliated on a SiO_2/ Si substrate by the Scotch tape method. The electrodes were patterned by photolithography, followed by e-beam evaporation of Ti/Pt (15/10 nm). An exfoliated WSe_2 layer was transferred onto the device region by the poly(methyl methacrylate) (PMMA)-transfer method,[28] resulting in the formation of a WSe_2/MoS_2 heterostructure and the contact of WSe_2 with the Pt electrode. Figure 1b shows an optical image of the fabricated dual-channel device. It should be noted that the bottom MoS_2 layer is contacted by the Ti electrodes, while the top WSe_2 layer has direct contact with the Pt electrodes, as shown in Figure 1c. The band diagrams for the WSe_2–Pt metal and MoS_2–Ti metal are illustrated in Figure 1d. Typically, Ti has been used as the metal contacts for conventional MoS_2 FETs, since the small work function of Ti (4.1 eV) results in a lower contact barrier to the conduction band (CB) of MoS_2, resulting in n-type transport in the MoS_2 FETs.[29] Meanwhile, the Fermi level of Pt with a larger work function (5.9 eV) is close to the valence band (VB) of WSe_2, leading to p-type transport in the WSe_2 FETs.[30] In such a manner, ambipolar transport can be achieved in the

dual-channel heterostructure by transport of electrons (holes) in the independent channel layer of MoS_2 (WSe_2), as illustrated in Figure 1c.

To investigate the optical properties of the WSe_2/MoS_2 heterostructure, Raman spectroscopy was employed using a laser with a wavelength of 532 nm. The optical microscopy images in **Figure 2**a show the three different positions selected for measurement. The Raman spectra of Figure 2b show that there are three dominant Raman peaks at 254 cm^{-1} (out-of-plane A_{1g} mode), 261 cm^{-1} (second-order Raman scattering mode 2LA(M)), and 310 cm^{-1} (inactive B^1_{2g} mode), as previously observed.[31] From the frequency difference (24 cm^{-1}) of the in-plane E^1_{2g} mode and out-of-plane A_{1g} mode in the Raman spectrum of MoS_2 (position 2), the thickness of the underlying MoS_2 was estimated to be four layers (see Figure S2a, Supporting Information, for detailed analysis of MoS_2 Raman spectra).[32] In the overlapped WSe_2/MoS_2 region (position 3), the Raman peak intensities of both MoS_2 and WSe_2 decreased due to the quenching effect.[33] The Raman mapping in Figure 2c,d was performed at 254 and 386 cm^{-1}, which correspond to the A_{1g} mode of WSe_2 and the E^1_{2g} mode of MoS_2, respectively. From the mapping images, the area of WSe_2/MoS_2 heterostructure can be clearly distinguished. The lowered Raman intensity of WSe_2 (blue area) in Figure 2c again confirms the quenching effect in the overlapped WSe_2/MoS_2 area.

To study the optoelectronic interactions in the heterostructure, photoluminescence (PL) measurements were performed using a laser with a wavelength of 514 nm. The PL spectra of Figure 2e were obtained from the three different positions indicated in Figure 2a. A broad PL peak of WSe_2 was observed at 1.56 eV for both regions of WSe_2 and the overlapped WSe_2/MoS_2. Two PL peaks of WSe_2 from indirect transitions (I) and A excitons (A) can be separated by fitting the broad peak with two Lorentzian curves (see Figure S2b, Supporting Information),
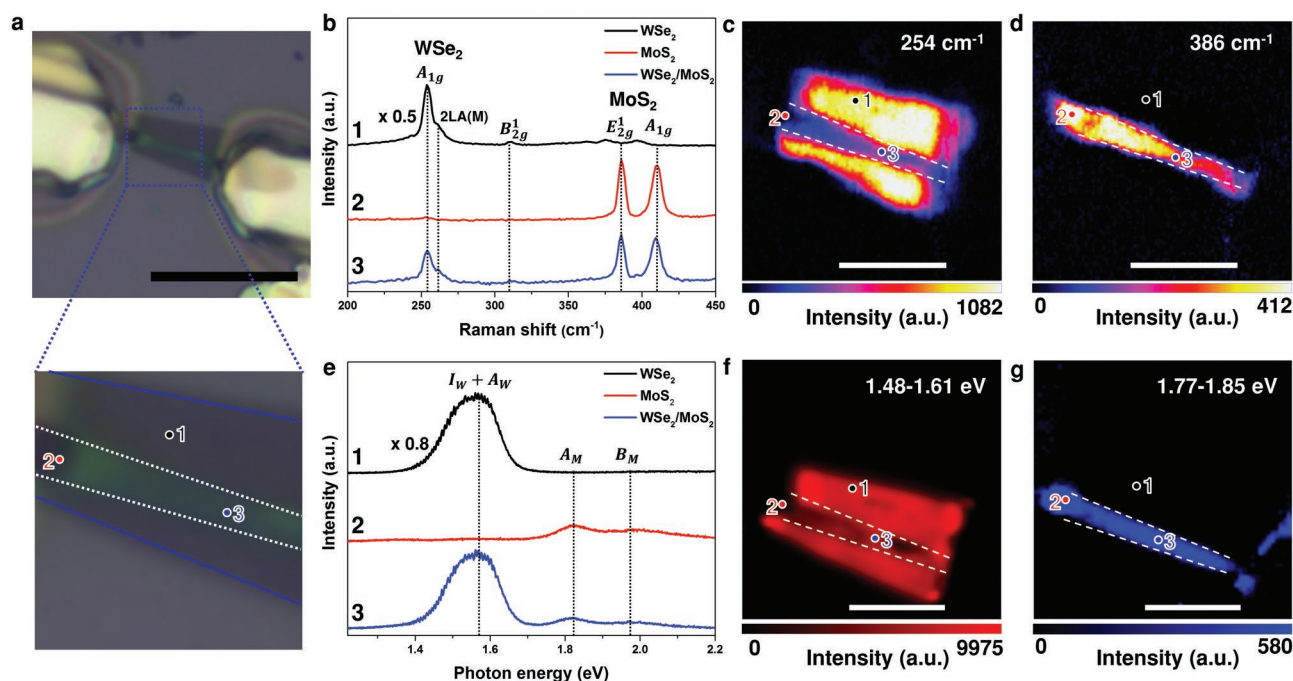
Figure 2. Optical investigation of the WSe$_2$/MoS$_2$ heterostructure. a) Optical images of the fabricated dual-channel device (top) and enlarged channel area (bottom). The numbers indicate three positions where the Raman and PL spectra were extracted. (Position 1: WSe$_2$, position 2: MoS$_2$—region of partial peeling off of PMMA/WSe$_2$ layers near the metal edge, position 3: overlapped WSe$_2$/MoS$_2$.) The scale bar indicates 10 μm. The white dashed line represents the bottom MoS$_2$ layer. b) Raman spectra of the indicated positions in (a). The intensity of the WSe$_2$ spectrum was reduced by a factor of 0.5. c,d) Raman mapping images for WSe$_2$ (c) and MoS$_2$ (d). The wavenumbers of 254 and 386 cm^{-1} were selected for WSe$_2$ and MoS$_2$, respectively. e) PL spectra at the different positions in (a). The intensity of WSe$_2$ was reduced by a factor of 0.8. f,g) PL mapping images for WSe$_2$ (f) and MoS$_2$ (g). The PL mapping was measured with photon energies of 1.48–1.61 eV for WSe$_2$ and 1.77–1.85 eV for MoS$_2$, respectively.

resulting in an I_W peak at 1.52 eV and A_W peak at 1.59 eV, in good agreement with the PL spectra of bilayer WSe$_2$.[34] The measured indirect bandgap of MoS$_2$ from the PL spectrum of MoS$_2$ is 1.37 eV (see Figure S2c, Supporting Information), which corresponds to the I peak of four-layer MoS$_2$ (I_M). The PL mapping was performed with photon energies of 1.48–1.61 eV (I_W and A_W peaks) for WSe$_2$ and 1.77–1.85 eV (A_M peak) for MoS$_2$. From the PL mapping image and PL spectrum of the overlapped WSe$_2$/MoS$_2$ region, a quenching effect was also observed, as seen in the Raman results in our experiment and reported previously.[14,33] It should be noted that the quenching of the individual PL intensities of WSe$_2$ and MoS$_2$ originates from interlayer coupling, which causes recombination of excitons at the heterointerface.[15,33] The enlarged PL spectra in Figure S2d (Supporting Information) show that the two peaks at 1.82 and 1.99 eV correspond to PLs from the A exciton (A_M) and B exciton (B_M) of MoS$_2$, respectively.

Before measurement of the dual-channel WSe$_2$/MoS$_2$ FETs, the single-channel FETs of MoS$_2$ and WSe$_2$ were separately measured to confirm the doping polarity in each channel material, as shown in Figure S3 (Supporting Information). The transfer characteristics of the single-channel MoS$_2$ (WSe$_2$) FET with Ti (Pt) electrodes showed n-type (p-type) unipolar transport. Meanwhile, the I_D–V_G characteristics of the dual-channel WSe$_2$/MoS$_2$ heterostructure FET are shown in **Figure 3**a,b, and we clearly observe ambipolar behavior, which is attributed to electron transport through the MoS$_2$ channel and hole transport through the WSe$_2$ channel. The on/off ratio of hole conduction

was enhanced ≈10 000 times by adding the p-type channel, as shown in the inset of Figure 3a. Normally, ambipolar transport in TMD FETs is achieved by using the ionic-gate technique[35] or contact-engineered thick TMDs[36] to enhance the electron (hole) conduction for WSe$_2$ (MoS$_2$) FET. However, we have obtained ambipolar behavior in the WSe$_2$/MoS$_2$ heterostructure while: i) preserving the atomic thickness and ii) using conventional SiO$_2$/Si back-gate structure. This observation of ambipolar transport would facilitate future studies based on exciton coupling and superfluidity in atomic-scale heterostructure. Recently, a black-phosphorus-based FET[37] was also investigated with ambipolar behavior, but the narrow off-current region, similar to graphene, prohibits digital or logical applications, where a wide off-state window is required. Our dual-channel heterostructure offers a reasonably wide off-state window of ≈28 V (depletion area, as shown in Figure 3b) and therefore provides a healthy margin for logic-circuit applications. Furthermore, this off-state window can be modulated by doping level or alignment of different band gap energies of MoS$_2$ and WSe$_2$ (see Section S4–S6 and Figure S5–S10, Supporting Information, for additional fabricated dual-channel FETs).

The field-effect mobilities of holes and electrons in the WSe$_2$/MoS$_2$ dual-channel FET were extracted at V_D = 1 V from the linear region of the transfer curve using the relation:

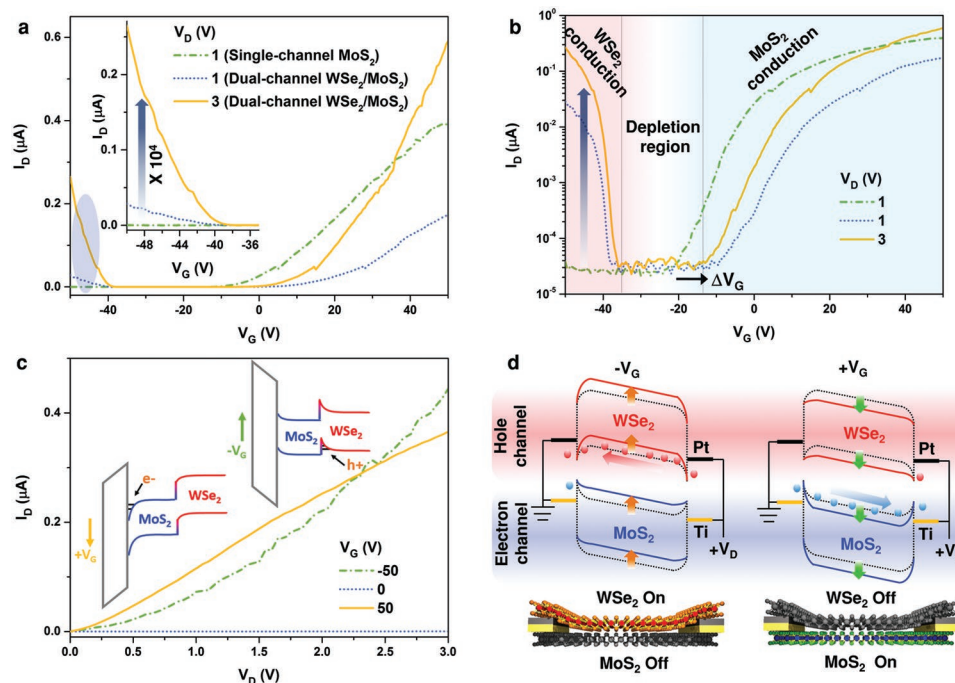$$\mu = \frac{L}{W}\left(\frac{dI_D}{dV_G}\right)\left(\frac{1}{C_i \times V_D}\right) \qquad (1)$$

COMMUNICATION

Figure 3. Electrical performance of the ambipolar dual-channel FET with WSe$_2$/MoS$_2$ heterostructure. a) I_D–V_G curves of single-channel MoS$_2$ FET before the transfer of WSe$_2$ layer (green: V_D = 1 V) and dual-channel WSe$_2$/MoS$_2$ FET (blue: V_D = 1 V, yellow: V_D = 3 V). The inset shows an enlarged plot of the hole-transport area. b) Logarithm-scale plot of (a). The gate voltage difference (ΔV_G) indicates a shift of threshold voltage (V_{th}) for n-type transport. c) I_D–V_D curves of the dual-channel WSe$_2$/MoS$_2$ FET measured at V_G = −50, 0, and 50 V. The insets show the vertical energy band diagrams at positive and negative V_G. d) Lateral band diagrams of the dual-channel WSe$_2$/MoS$_2$ FET at positive and negative V_G. The black dotted, black solid, and yellow solid lines indicate the band structure of the WSe$_2$/MoS$_2$ stack and Fermi levels of the Pt and Ti electrodes in the absence of gate bias, respectively. The red and blue solid lines show the shifted CB and VB energy levels for WSe$_2$ and MoS$_2$ at negative and positive V_G.

where L, W, and C_i are the channel length and width, and the capacitance per unit area, respectively. The extracted mobilities for MoS$_2$ and WSe$_2$ channels were 5.97 and 0.54 cm^2 V^{-1} s^{-1}, respectively. The rather low hole mobility in WSe$_2$ can be caused by screening of the gate field by the metal electrodes as WSe$_2$ was transferred on the top of the electrodes, which leads to an increase in the contact resistance. Figure 3c shows the well-established contact behavior for both the MoS$_2$ and the WSe$_2$ channels: detailed measurements are shown in Figure S4 (Supporting Information) (see Section S4, Supporting Information, for details). Although the work-function differences at the metal–semiconductor results in the formation of a small Schottky barrier height at the contacts, carrier injection assisted by thermionic field emission results in a quasi-Ohmic behavior at room temperature. Moreover, in the accumulation mode (V_G = −50 and +50 V for WSe$_2$ and MoS$_2$, respectively, as shown in Figure 3c), the contact behavior is further enhanced due to reduced barrier width and efficient carrier tunneling at the contacts. In contrast, for zero gate bias, a relatively small current was obtained due to the planar p–n junction formation at the heterointerface, which reduces the carrier concentration in both layers. The schematic energy-band diagrams illustrated in the insets of Figure 3c (vertical direction) and in Figure 3d (lateral direction) present the modulation of ambipolar behavior by an applied gate bias. The polarity of the majority charge carriers can be controlled by tuning the Fermi levels of MoS$_2$ and WSe$_2$ relative to the edges of the CB of

MoS$_2$ (for n-type state) and VB of WSe$_2$ (for p-type state) by a gate bias. The CB minima and VB maxima of WSe$_2$ and MoS$_2$ shift upward for V_G < −40 V, leading to the accumulation of holes in the VB of WSe$_2$ and depletion of electrons in the CB of MoS$_2$. On the other hand, for V_G > −15 V, the energy bands shift downward, resulting in accumulation of electrons in the CB of MoS$_2$ and depletion of holes in the VB of WSe$_2$. The carrier-depletion effect of the planar p–n junction formation can also be seen from the threshold voltage (V_{th}) shift of the MoS$_2$ layer. The carrier density depleted in the MoS$_2$ channel by the top WSe$_2$ layer can be calculated by $Q_D = C_i \times \Delta V_{th}/q$, where Q_D, C_i, q, and ΔV_{th} are the depletion charge density, capacitance, charge, and threshold voltage shift, respectively. The calculated Q_D is ≈9.41 × 10^{11} cm^{-2}, which also correlates well with the top-gate induced depletion in the double-gated MoS$_2$ FET at V_{TG} = −2.5 V, as shown in Figure S11 and S12 (Supporting Information) (see Section S8, Supporting Information, for details).

To investigate the photoresponse of the dual-channel WSe$_2$/MoS$_2$ FET, the photoinduced current was measured under laser illumination with various photon energies. The device was illuminated with a power density of 1 mW cm^{-2}. The recombination and generation at the lateral heterointerface play an important role in determining the total photocurrent response, especially the gate dependence of the photoresponse. Therefore, in the fabricated dual-channel WSe$_2$/MoS$_2$ FET, this dominant photoactive area of the overlapped MoS$_2$

Materials
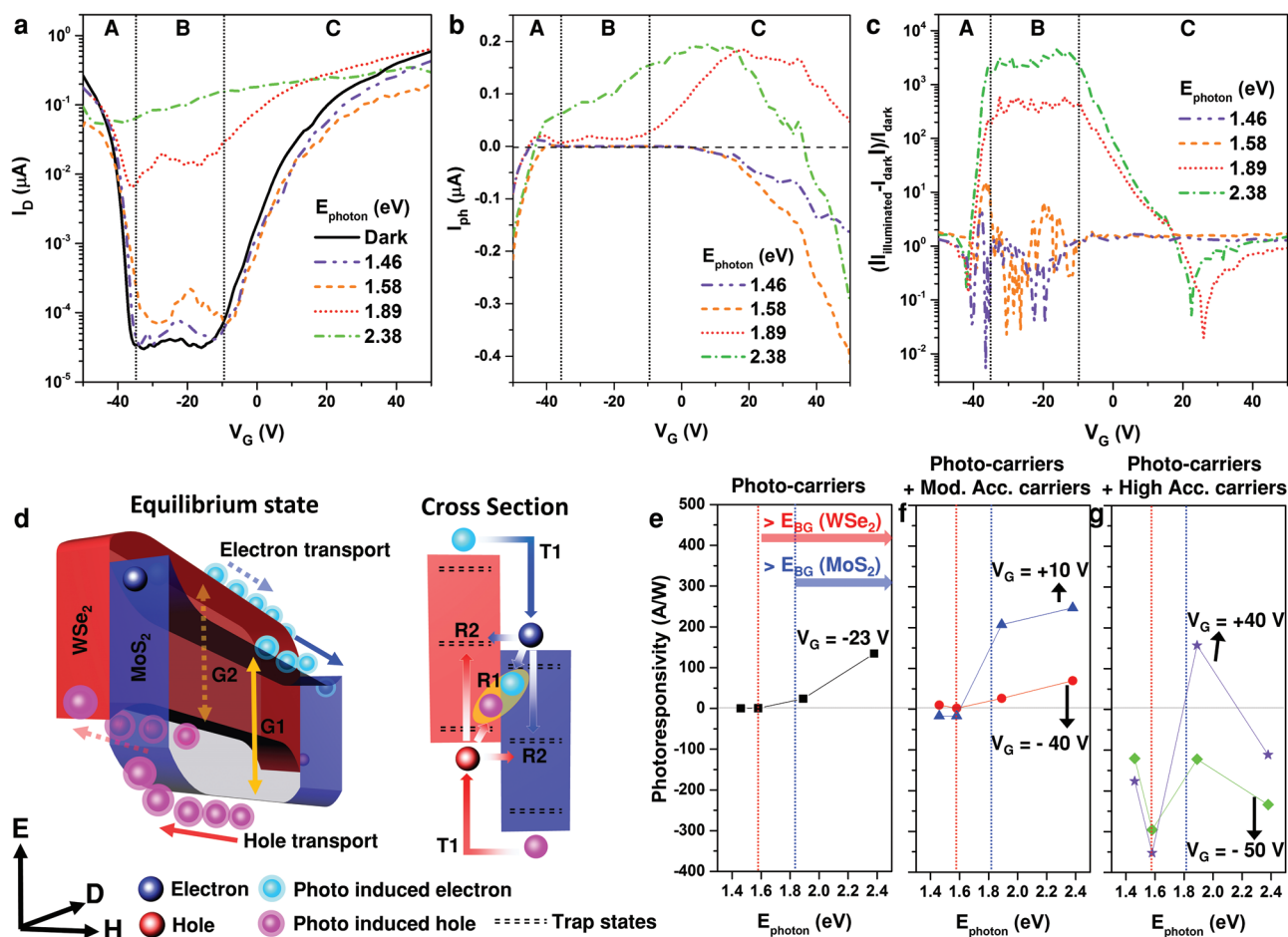Views
www.MaterialsViews.com

ADVANCED
MATERIALS
www.advmat.de

COMMUNICATION

Figure 4. Photoresponse of dual-channel FET with WSe$_2$/MoS$_2$ heterostructure. a) I_D–V_G curves at V_D = 3 V under laser illumination of photon energies of 2.38, 1.89, 1.58, and 1.46 eV. b) I_{ph}–V_G curves obtained from (a). c) Normalized photocurrent. d) (Left) Band diagram for equilibrium state of dual-channel FET and (right) the cross section band diagram to show the possible recombination processes. The E, D, and H letters in the arrow in axis indicate the energy level, channel distance, and height, respectively. The dotted arrow and solid line arrow represent the movement of hole and electrons in WSe$_2$ and MoS$_2$. Photoresponsivity as function of various photon energies at gate bias of e) −23 V, f) +10, −40 V, and g) +40, −50 V.

and WSe$_2$ was considered as the active area. The observed optical bandgap energies of WSe$_2$ and MoS$_2$ are 1.59 and 1.82 eV, corresponding to A exciton energies as shown in Figure S2b,d (Supporting Information). Therefore, the obtained photoresponse can be interpreted by comparing the illuminated laser energies with the optical bandgap energies of WSe$_2$ and MoS$_2$. **Figure 4**a shows the I_D–V_G characteristics with laser wavelengths of 520, 655, 785, and 850 nm, which correspond to photon energies of 2.38, 1.89, 1.58, and 1.46 eV, respectively. In order to obtain the photocurrent (I_{ph}) from Figure 4a, the illuminated current was subtracted by dark current, and plotted in Figure 4b. As increasing the photon energy from 1.46 to 1.58 eV, the V_{th} was slightly shifted to the positive-gate-bias region, while a shift to the negative-gate-bias region was observed for 1.89 and 2.38 eV. This behavior clearly indicates the photogating effect which means that the generated photocarriers can be positioned in trap states caused by structural defect and absorbed oxygen molecules on the surface (see Section S9, Figure S13–S15, and Table S1 and S2, Supporting Information, for details of the photoresponse properties and

summarized device characteristics of the fabricated devices in this study). Further, the normalized photocurrent was calculated to illustrate the change of photocurrent relative to the dark current, by subtracting and dividing the dark current from the current under illumination, as shown in Figure 4c. Figure 4a–c can be divided into three regions based on electrical conduction, where A, B, and C represent the hole current (WSe$_2$ channel), off-current (depletion region), and electron current (MoS$_2$ channel), respectively. Generally, at the off-current region without illumination, the electrons (holes) from MoS$_2$ (WSe$_2$) are unable to flow due to high electron (hole) barrier height. Under illumination, the electron and hole pairs can be generated as shown in the left schematic diagram of Figure 4d (the G1 and G2 indicate the photocarrier generation process in WSe$_2$ and MoS$_2$ layer); consequently, the off-current can be increased with flow of photoinduced carriers. For photon energies of 1.46 and 1.58 eV, an overall lower photocurrent was obtained with no discernible increase in the region B, with very high negative photocurrent at extreme gate bias, whereas for photon energies of 1.89 and 2.38 eV, which

COMMUNICATION

have the higher energies than the bandgap of MoS_2 and WSe_2, a higher photocurrent was maintained throughout the gate bias except at the extreme gate-bias regime (Region A and C), where a considerable drop in the photocurrent was observed. In order to explain the dropping of the photoresponse behavior according to the carrier concentration, the photoresponsivity, $R = I_{ph}/P_{in}$ where I_{ph} and P_{in} are the photocurrent and incident optical power (≈ 1 nW), was calculated for low, moderate, and high carrier-accumulation regions, as shown in Figure 4e. The photoresponsivity in the low and moderate carrier-accumulation regions (low: $V_G = -23$ V, moderate: $V_G = -40$ and +10 V for WSe_2 and MoS_2) shows gradually increasing behavior when the photon energies are higher than bandgap (E_{BG}) of the materials. Especially, in the high carrier-accumulation region ($V_G = -50$ and +40 V for WSe_2 and MoS_2), a huge negative photoresponsivity was observed for both regions excepting the values of MoS_2 at a photon energy of 1.89 eV. The possible reasons behind this dropping of photocurrent in the extreme gate bias (high carrier accumulation) for almost all the photon energies can be understood from the dynamic balance between the recombination and generation rate. The generation rate is independent of the gate bias, whereas the recombination rate has critical dependence on the gate bias as a function of Fermi level shift in the bandgap, which influences the defects/impurities states, thus affecting the overall photoresponse in the device. In particular, in the high gate-bias regime, the movement of the quasi-Fermi level toward the conduction (valence) band activates the defects/impurities states, which results in higher recombination rate due to their short lifetime.[38] Of various radiative (band-to-band and Langevin) and non-radiative (Shockley–Read–Hall and Auger) recombination processes, the device photoresponse depends upon the dominant recombination process, which in turn depend upon the carrier concentration, defects/traps density and energies, incident power, and layer thickness. In our device, an added recombination route at the WSe_2/MoS_2 heterointerface further enhanced the recombination probability, thus giving rise to a higher negative photocurrent compared to single-material devices observed elsewhere.[39] To summarize the above discussion, the possible recombination processes of a heterostructure device are shown in the right schematic diagram of Figure 4c. Further, the R1, R2, and T1 indicate the Langevin and SRH recombination processes, and possible path of carrier transfer in our device structure, respectively. Such non-radiative recombination also induces phonon scattering, which is further aggravated by the scattering due to additional gate-induced carriers and ultimately results in the decrease of carrier mobility, thus the decline in the photocurrent at the extreme gate bias.[40] This can be evident from the abnormal photoresponse for 2.38 eV where a negative photocurrent was observed due to the higher density of photoinduced carriers, which, when combined with the above-discussed scattering and recombination mechanism, resulted in negative photocurrent at extreme gate bias, whereas for 1.89 eV, an optimum equilibrium between the generation and recombination process was maintained resulting in an overall positive photocurrent, with a gradual decline in the extreme gate bias regime for the reasons discussed above.

In conclusion, a dual-channel FET was fabricated by vertically stacking p-type WSe_2 and n-type MoS_2 atomically thin layers.

The combined effect of unipolar single-channel TMDs enables an ambipolar property in the integrated heterostructure device. The electron and hole transport can be selected as controlling the gate bias. In the photoresponse study, a large negative photocurrent was observed, and it can be tuned by modulating the photon energy and gate bias to gain the positive photocurrent. The vertically stacked p- and n-channel heterostructure reduces device fabrication complexities, specifically for ambipolar CMOS invertors. The dual-channel FET demonstrates novel optoelectrical applications of TMDs in stacked 2D materials to achieve highly dense electronics. Moreover, in the near future, the extension of exciton-related study in p- and n-type stacked heterostructures can be realized with a similar structure to that achieved in this study.

Experimental Section

Single-Channel MoS_2 FET Fabrication: MoS_2 was exfoliated on a cleaned 300 nm thick SiO_2/Si substrate and identified by using Raman spectroscopy. On the exfoliated MoS_2, electrodes were patterned by photolithography and deposition of Ti (15 nm) and Pt (10 nm). To enhance the electrical contact, the fabricated devices were annealed at 180 °C under vacuum condition for 10 min.

Transfer Technique in Fabrication of the Dual-Channel WSe_2/MoS_2 FET: After fabrication of the single-channel MoS_2 FET, a WSe_2 layer was transferred onto the channel area of the MoS_2 FET, including a Pt electrode. For the transfer technique, the conventional layer transfer method was used. The WSe_2 layer was exfoliated on PMMA/poly(vinyl alcohol) (PVA)-coated Si substrate. A thin layer with a pale color was identified with an optical microscope and marked with a pen. Then the WSe_2/PMMA/PVA/Si substrate was floated on water. After dissolving the PVA layer in the water, the WSe_2/PMMA layer was detached from the Si substrate. The WSe_2/PMMA layer was picked up by a home-made plate with a hole around 1 mm. Finally, the WSe_2/PMMA layer was transferred onto the MoS_2 FET or onto a SiO_2/Si wafer, using a microscope for alignment.

Characterization with PL and Raman Spectroscopy: To characterize the MoS_2 and WSe_2 electronic structure, PL and Raman spectroscopy were used with laser wavelengths of 514 and 532 nm, respectively.

Electrical Measurement with Laser Illumination: In order to characterize the electrical properties of FETs, three-terminal measurement was performed in a dark environment at room temperature. To observe the photoresponse, the device was illuminated by laser light with a power density of 1 mW cm^{-2} and wavelengths of 520, 655, 785, and 850 nm.

Supporting Information

Supporting Information is available from the Wiley Online Library or from the author.

Acknowledgements

[1] A. K. Geim, K. S. Novoselov, *Nat. Mater.* **2007**, *6*, 183.

[2] C. Lee, X. Wei, J. W. Kysar, J. Hone, *Science* **2008**, *321*, 385.

[3] K. S. Kim, T. Zhao, H. Jang, S. Y. Lee, J. M. Kim, K. S. Kim, J. H. Ahn, P. Kim, J. Y. Choi, B. H. Hong, *Nature* **2009**, *457*, 706.

[4] D. Jariwala, V. K. Sangwan, L. J. Lauhon, T. J. Marks, M. C. Hersam, *ACS Nano* **2014**, *8*, 1102.

[5] Y. Lee, J. H. Ahn, *Nano* **2013**, *8*, 1330001.

[6] O. Lopez-Sanchez, D. Lembke, M. Kayci, A. Radenovic, A. Kis, *Nat. Nanotechnol.* **2013**, *8*, 497.

[7] S. Jo, N. Ubrig, H. Berger, A. B. Kuzmenko, A. F. Morpurgo, *Nano Lett.* **2014**, *14*, 2019.

[8] X. Cui, G. H. Lee, Y. D. Kim, G. Arefe, P. Y. Huang, C. H. Lee, D. A. Chenet, X. Zhang, L. Wang, F. Ye, F. Pizzocchero, B. S. Jessen, K. Watanabe, T. Taniguchi, D. A. Muller, T. Low, P. Kim, J. Hone, *Nat. Nanotechnol.* **2015**, *10*, 534.

[9] M. Levendorf, C. J. Kim, L. Brown, P. Y. Huang, R. W. Havener, D. A. Muller, J. Park, *Nature* **2012**, *488*, 627.

[10] Y. Gong, J. Lin, X. Wang, G. Shi, S. Lei, Z. Lin, X. Zou, G. Ye, R. Vajtai, B. I. Yakobson, H. Terrones, M. Terrones, B. K. Tay, J. Lou, S. T. Pantelides, Z. Liu, W. Zhou, P. M. Ajayan, *Nat. Mater.* **2014**, *13*, 1135.

[11] S. Rathi, I. Lee, D. Lim, J. Wang, Y. Ochiai, N. Aoki, K. Watanabe, T. Taniguchi, G. H. Lee, Y. J. Yu, P. Kim, G. H. Kim, *Nano Lett.* **2015**, *15*, 5017.

[12] H. Fang, C. Battaglia, C. Carraro, S. Nemsak, B. Ozdol, J. S. Kang, H. A. Bechtel, S. B. Desai, F. Kronast, A. A. Unal, G. Conti, C. Conlon, G. K. Palsson, M. C. Martin, A. M. Minor, C. S. Fadley, E. Yablonovitch, R. Maboudian, A. Javey, *Proc. Natl. Acad. Sci. USA* **2014**, *111*, 6198.

[13] D. Jariwala, V. K. Sangwan, C. C. Wu, P. L. Prabhumirashi, M. L. Geier, T. J. Marks, L. J. Lauhon, M. C. Hersam, *Proc. Natl. Acad. Sci. USA* **2013**, *110*, 18076.

[14] D. Jariwala, S. L. Howell, K. S. Chen, J. Kang, V. K. Sangwan, S. A. Filippone, R. Turrisi, T. J. Marks, L. J. Lauhon, M. C. Hersam, *Nano Lett.* **2016**, *16*, 497.

[15] C. Lee, G. H. Lee, A. M. van der Zande, W. Chen, Y. Li, M. Han, X. Cui, G. Arefe, C. Nuckolls, T. F. Heinz, J. Guo, J. Hone, P. Kim, *Nat. Nanotechnol.* **2014**, *9*, 676.

[16] M. L. Tsai, S. H. Su, J. K. Chang, D. S. Tsai, C. H. Chen, C. I. Wu, L. J. Li, L. J. Chen, J. H. He, *ACS Nano* **2014**, *8*, 8317.

[17] F. Withers, D. Pozo-Zamudio, A. Mishchenko, A. P. Rooney, A. Gholinia, K. Watanabe, T. Taniguchi, S. J. Haigh, A. K. Geim, A. I. Tartakovskii, K. S. Novoselov, *Nat. Mater.* **2015**, *14*, 301.

[18] U. Sivan, P. M. Solomon, H. Shtrikman, *Phys. Rev. Lett.* **1992**, *68*, 1196.

[19] A. Avsar, J. Y. Tan, T. Taychatanapt, J. Balakrishnan, G. K. W. Koon, Y. Yeo, J. Lahiri, A. Carvalho, A. S. Rodin, E. C. T. O'Farrell, G. Eda, A. H. C. Neto, B. Ozyilmaz, *Nat. Commun.* **2014**, *10*, 5875.

[20] R. V. Gorbachev, A. K. Geim, M. I. Katsnelson, K. S. Novoselov, T. Tudorovskiy, I. V. Grigorieva, A. H. MacDonald, S. V. Morozov, K. Watanabe, T. Taniguchi, L. A. Ponomarenko, *Nat. Phys.* **2012**, *8*, 896.

[21] E. Tutuc, M. Shayegan, D. A. Huse, *Phys. Rev. Lett.* **2004**, *93*, 036802.

[22] J. P. Eisenstein, A. H. MacDonald, *Nature* **2004**, *432*, 691.

[23] A. V. Balatsky, Y. N. Joglekar, B. Littlewood, *Phys. Rev. Lett.* **2004**, *93*, 266801.

[24] J. J. Su, A. H. MacDonald, *Nat. Phys.* **2008**, *4*, 800.

[25] A. Perali, D. Neilson, A. R. Hamilton, *Phys. Rev. Lett.* **2013**, *110*, 146803.

[26] M. M. Fogler, L. V. Butov, K. S. Novoselov, *Nat. Commun.* **2014**, *10*, 5555.

[27] Y. Zhang, J. Ye, I. Matsuhashi, Y. Iwasa, *Nano Lett.* **2012**, *12*, 1136.

[28] C. R. Dean, A. F. Young, C. Lee, L. Wang, S. Sorgenfrei, K. Watanabe, T. Taniguchi, P. Kim, K. L. Shepard, J. Hone, *Nat. Nanotechnol.* **2010**, *5*, 723.

[29] D. Saptarshi, H. Y. Chen, A. V. Penumatcha, J. Appenzeller, *Nano Lett.* **2012**, *13*, 100.

[30] I. Y. Lee, S. Rathi, L. Lijun, D. Lim, M. A. Khan, E. S. Kannan, G. H. Kim, *Nanotechnology* **2015**, *26*, 455203.

[31] W. Zhao, Z. Ghorannevis, K. K. Amara, J. R. Pang, M. Toh, X. Zhang, C. Kloc, P. H. Tan, G. Eda, *Nanoscale* **2013**, *5*, 8677.

[32] C. Lee, H. Yan, L. E. Brus, T. F. Heinz, J. Hone, S. Ryu, *ACS Nano* **2010**, *5*, 2695.

[33] M. H. Chiu, M. Y. Li, W. Zhang, W. T. Hsu, W. H. Chang, M. Terrones, H. Terrones, L. J. Li, *ACS Nano* **2014**, *9*, 9649.

[34] W. Zhao, Z. Ghorannevis, L. Chu, M. Toh, C. Kloc, P. H. Tan, G. Eda, *ACS Nano* **2013**, *7*, 791.

[35] A. Adrien, K. Andras, *ACS Nano* **2014**, *8*, 7180.

[36] D. Saptarshi, A. Joerg, *Appl. Phys. Lett.* **2013**, *103*, 103501.

[37] W. Zhu, M. N. Yogeesh, S. Yang, S. H. Aldave, J. S. Kim, S. Sonde, L. Tao, N. Lu, D. Akinwande, *Nano Lett.* **2015**, *15*, 1883.

[38] D. Kufer, G. Konstantatos, *Nano Lett.* **2015**, *15*, 7307.

[39] W. Zhang, J. K. Huang, C. H. Chen, Y. H. Chang, Y. J. Cheng, L. J. Li, *Adv. Mater.* **2013**, *25*, 3456.

[40] D. H. Kang, M. S. Kim, J. Shim, J. Jeon, H. Y. Park, W. S. Jung, H. Y. Yu, C. H. Pang, S. Lee, J. H. Park, *Adv. Funct. Mater.* **2015**, *25*, 4219.